


 HPSTAR
0121—2015

Electrical transport properties of AIs under compression: reversible boundary effect

 Cite this: *Phys. Chem. Chem. Phys.*,
2015, 17, 26277

 Jiejuan Yan,^a Feng Ke,^b Cailong Liu,^a Qinglin Wang,^b Junkai Zhang,^b Li Wang,^a
Gang Peng,^a Yonghao Han,^{*a} Yanzhang Ma^{bc} and Chunxiao Gao^{*a}

Herein, we report on the intriguing electrical transport properties of compressed AIs. The relative permittivity and the resistances of both the grain and bulk boundaries vary abnormally at ~ 10.9 GPa, accompanied by the cubic–hexagonal structural transition of AIs. With further compression, the boundary effect becomes undistinguished, and subsequently, the electrical transport mechanism converts from boundary- to bulk-dominated, which gives rise to a significant reduction in the total resistance of AIs. After being quenched to ambient pressure, resistances recover to the initial values followed by the re-emergence of the boundary effect. E_g decreases with pressure and its pressure dependence changes at ~ 14.0 GPa, which rationalizes the anomalous variation of the electrical transport properties. The experimental results indicate that the boundary effect can be modulated by compression and increases the resistance difference between the two states. This opens up a new possible basis for optimizing the performance of AIs-based applications, including multilevel phase-change memories.

 Received 26th June 2015,
Accepted 4th September 2015

DOI: 10.1039/c5cp03706a

www.rsc.org/pccp

1. Introduction

As is well known, grain boundaries are usually undesired in many applications because they can heavily affect the electrical transport, mechanical and optical properties of materials such as carrier concentration, mobility and electrical conductivity.^{1–5} Numerous studies are therefore focused on minimizing or eliminating such undesirable effects of grain boundaries. Several approaches, such as improving the quality of crystalline materials^{6,7} and intentional doping,^{8,9} are applied to minimize the influence of grain boundaries on electronic devices. On the other hand, a few efforts have been made recently to apply the grain boundary effect to optimize the performance of electronic devices. For instance, by introducing grain boundaries as switchable transport channels, Yasaei *et al.*³ improved the chemical sensing of graphene-based electronic devices. Kim *et al.*¹⁰ reduced the thermal conductivity of thermoelectric materials by improving the dislocation arrays at grain boundaries to scatter mid-frequency phonons. Herein, we report that the grain boundary electrical transport properties can be modulated by compression and are reversible during decompression, which significantly increase the resistance difference between two states.

AIs is a narrow band-gap semiconductor belonging to the group III–V family that has attracted extensive interest due to its practical applications, including hetero-junction bipolar transistors and high electron mobility transistors.^{11–15} Under ambient conditions, it crystallizes into a face-centered cubic structure with $F\bar{4}3m$ symmetry (designated as B3 type).¹⁶ There have been two prior studies on the structural properties of AIs under compression: one illustrated that it transformed into the NiAs structure (B8) under pressure;^{17,18} the other proposed that it went through the B3–B1 structural transition^{19–21} and behaves as a metal in its high-pressure phases. Although exploring the metallic state of AIs is a matter of interest in band-gap engineering, experimental evidence for whether AIs is metallic on high-pressure B8 and B1 phases remains unsettled. Moreover, the effect of grain boundaries on the electrical transport properties of AIs is still not fully understood, limiting the optimization of AIs-based applications.

An effective *in situ* approach to study the bulk and grain boundary electrical transport properties is the alternate current (AC) technique, *i.e.*, frequency-dependent complex impedance spectral analysis, by which one can clearly distinguish the contributions of bulk and grain boundary effects due to their different electrical responses under AC excitation signals. Furthermore, X-ray diffraction (XRD) is of great importance to make *in situ* observations of the structural transitions for rationalizing the anomalous variations of the electrical transport properties of AIs. By combining these measurements, we studied the effect of grain boundaries on the electrical transport properties of AIs under compression.

^a State Key Lab for Superhard Materials, Institute of Atomic and Molecular Physics, Jilin University, Changchun 130012, China. E-mail: cc060109@qq.com, hanyh@jlu.edu.cn

^b Center for High Pressure Science and Technology Advanced Research, Shanghai 201203, China

^c Department of Mechanical Engineering, Texas Tech University, Lubbock, TX79409, USA

2. Experimental section

The alternating current impedance spectral measurements involve an AC source signal, $U(\omega, t) = U_0 \cos(\omega t)$, loaded onto a sample, and a response current signal determined as $I(\omega, t) = I_0 \cos(\omega t - \gamma)$.²² The complex impedance is obtained by $Z^* = U/I = Z' + iZ''$, where the real (Z') and imaginary parts (Z'') are defined as the impedance fractions in and $\pm\pi/2$ out of the phase of $U(\omega, t)$, respectively. In our measurements, a two-electrode configuration microcircuit, wherein the sidewall of the sample chamber is one electrode and a Mo film microcircuit integrated on diamond surface is the other, was employed to measure the impedance spectra of ALAs. The integration process of the Mo film microcircuit can be found from a previously reported study.²³ Fig. 1 illustrates the sectional view of the Mo film microcircuit. T-301 stainless steel was pre-indented to 40 μm , and then insulated with a mixture of diamond powders and epoxy. Subsequently, a hole with 100 μm in diameter was drilled in the center of the indentation by a laser drilling machine and used as the sample chamber. Powdered ALAs samples (bought from Alfa Aesar Co. with purity of 99.5%) and small piece of ruby as the pressure calibrant²⁴ were then loaded into the sample chamber. To avoid introducing impurities and ensure good electrical contact, no pressure transmitting medium was loaded. The impedance spectra were obtained using a computer-controlled impedance analyzer (Solartron 1260) combined with a dielectric interface (Solartron 1296). A voltage signal with amplitude of 2 V, and frequency ranging from 0.01 to 10^7 Hz was applied to the sample.

Temperature dependent impedance spectral measurements were obtained by placing the diamond-anvil cells (DAC) into a heating cabinet for more than 10 min to achieve thermal equilibrium. Temperature was monitored by a standard thermocouple in contact with diamond.

In situ high-pressure XRD experiments were conducted at BL15U1 of the Shanghai Synchrotron Radiation Facility (SSRF) and BLAW2 of the Beijing Synchrotron Radiation Facility (BSRF) using the angle-dispersive XRD mode ($\lambda = 0.6199 \text{ \AA}$). The instrument parameters, including the distance between sample and detector, were calibrated using the CeO_2 standard material. XRD patterns were fitted by Rietveld refinement on the GSAS program package.²⁵

3. Results and discussion

Fig. 2(a)–(e) illustrate the Z'' – Z' plots of impedance spectra. Under ambient conditions, two components can be observed in

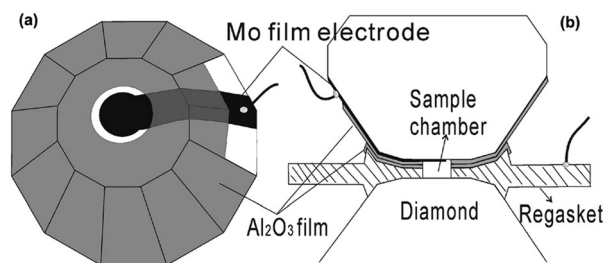


Fig. 1 (a) Configuration of the film microcircuit on diamond anvil cells. (b) Cross section of the designed DAC.

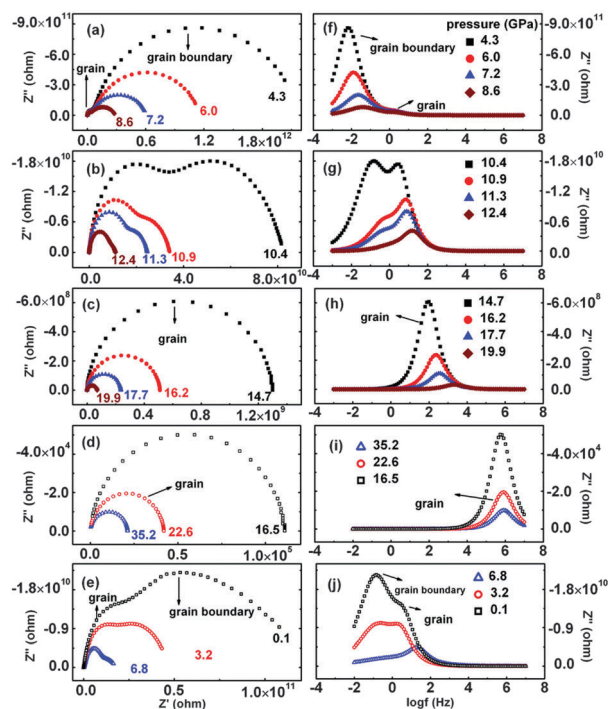


Fig. 2 The Z'' – Z' plots (a)–(e) and Z'' – f plots (f)–(j) of the impedance spectra of ALAs under compression. Solid and open symbols represent the data collected under the compression and decompression processes, respectively.

our results, in which the left (high-frequency) and right (low-frequency) components describe the bulk and grain boundary contributions, respectively.^{26,27} From ambient to 10.9 GPa, the components corresponding to the bulk effect are smaller than those of the grain boundaries, indicating that the grain boundary effect dominates the electrical transport properties of ALAs. However, in a pronounced conversion, the components related to the grain boundaries are dramatically reduced and become smaller than those of the bulk above 10.9 GPa. With further compression, a simple arc related to the bulk electrical response is observed, indicating that the undesirable hindering effect of the grain boundaries is much weaker and can be ignored compared to the bulk effect; *i.e.*, applying compression modulates the grain boundary effect successfully and drives the conversion of the electrical transport mechanism from grain boundary-dominated to bulk-dominated.

This pressure-driven conversion of the electrical transport mechanism can be further revealed by the Z'' – f plots of the impedance spectra. In Z'' – f patterns, the position and intensity of the relaxation peaks describe the type and strength of the electrical relaxation processes in the samples, respectively.²⁸ As shown in Fig. 2(f)–(h), the relaxation peaks of the grain boundary effect lose their intensities rapidly with increasing pressure. Above 12.4 GPa, the relaxation peaks related to the grain boundary effect disappear but those of the bulk effect stay robust, which further confirm that the grain boundary effect on total electrical transport properties is suppressed.

To quantify the pressure effect on the electrical transport properties of ALAs, the impedance spectra were fitted with a

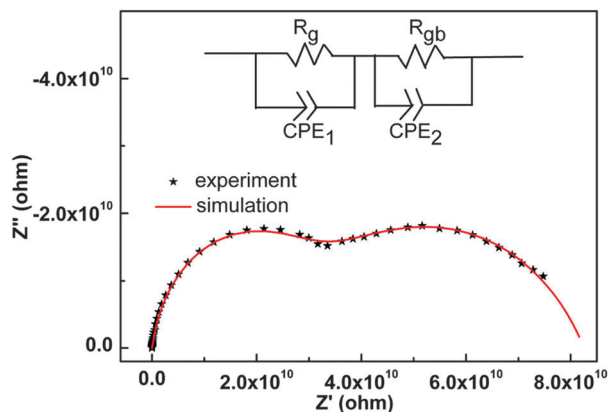


Fig. 3 Equivalent circuit describing the bulk and grain boundary electrical transport behaviors of AlAs under compression.

commonly used equivalent circuit model (Fig. 3) on the Zview2 impedance analysis software. Two parallel resistors (R) and constant-phase elements (CPE) were used to describe the bulk and grain boundary relaxation processes, respectively. The obtained bulk and grain boundary resistances (R_b , R_{gb}) and related relaxation frequencies (f_b , f_{gb}) are plotted in Fig. 4. In the low-pressure range (< 10.9 GPa), the resistances of both the bulk and grain boundaries vary smoothly with increasing pressure. However, R_b drops rapidly with further compression, followed by a change in pressure dependence. Above 14.7 GPa, R_b decreases linearly with pressure up to 38.1 GPa, the highest pressure of this measurement. These variations can be more

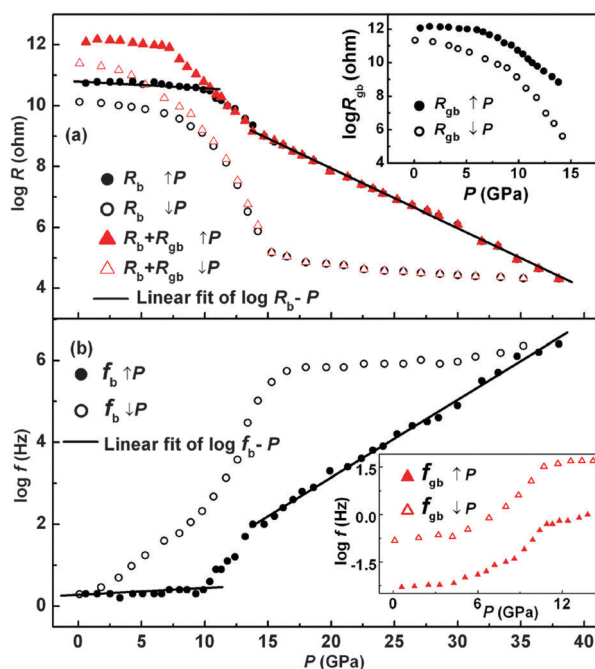


Fig. 4 (a and b) Pressure dependence of total resistance ($R_t = R_b + R_{gb}$), bulk resistance (R_b), and bulk relaxation frequency (f_b) of AlAs in compression and decompression runs. The insets (a) the pressure dependence of the grain boundary resistance (R_{gb}) and (b) the pressure evolution of the grain boundary relaxation frequency (f_{gb}).

clearly illustrated in the slope of $\log R_b - P$ plots. By linearly fitting the $\log R_b - P$ curves, the obtained slope is $-0.027 \Omega \text{ GPa}^{-1}$ below 10.9 GPa, but drops dramatically to $-0.197 \Omega \text{ GPa}^{-1}$ above 14.7 GPa. In the case of R_{gb} , it decreases markedly and becomes undistinguished due to the loss of the grain boundary electrical response above 14.7 GPa. The relaxation frequencies of bulk and grain boundaries, f_b and f_{gb} , show anomalous variations from ~ 10.9 to ~ 14.7 GPa. During the decompression, the components corresponding to the bulk effect (Fig. 2(d)–(e)) expand gradually with decreasing pressure. R_b increases dramatically below 14.2 GPa and goes back to its original state with quenching pressure to ambient. Moreover, the grain boundary effect reappears at ~ 14.2 GPa. R_{gb} increases sharply with decreasing pressure, and almost returns to its initial value with quenching to ambient pressure. The behaviors of f_b and f_{gb} track the changes in the compression run. The slight differences in values of R_{gb} and f_{gb} can be attributed to the lattice relaxation after a pressure cycle. Therefore, it is reasonable to consider that the bulk and grain boundary effects experience a reversible process in the whole compression run. Interestingly, it is found that the grain boundary electrical transport can be modulated significantly and further increases the difference between the high-resistance and low-resistance states, which is favored in phase-change memory materials.^{29,30}

In addition, from the impedance data, we can obtain the dielectric properties of AlAs under compression using the following relation:^{24,31}

$$\epsilon_r(P) = 1/2\pi\epsilon_0\rho f_{\max} \quad (1)$$

where ρ is the resistivity and ϵ_0 is the vacuum permittivity. Fig. 5 shows the pressure dependence of ϵ_r up to 38.1 GPa. At ambient pressure, the obtained ϵ_r of AlAs is 1337.9, which is large compared with the intrinsic value (10.06).³² However, our observation may involve extrinsic mechanisms, such as the grain boundary barrier layer capacitance effect and spatial inhomogeneity of the local dielectric response, instead of the intrinsic features of AlAs.³³ The ϵ_r of AlAs changes slightly as the pressure changes from ambient to 10.9 GPa, followed by a noticeable reduction at ~ 10.9 GPa and a slight decrease above

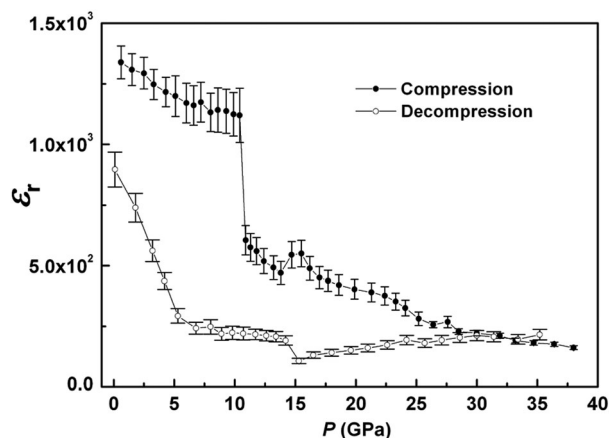


Fig. 5 Variation of the relative permittivity of AlAs under pressure.

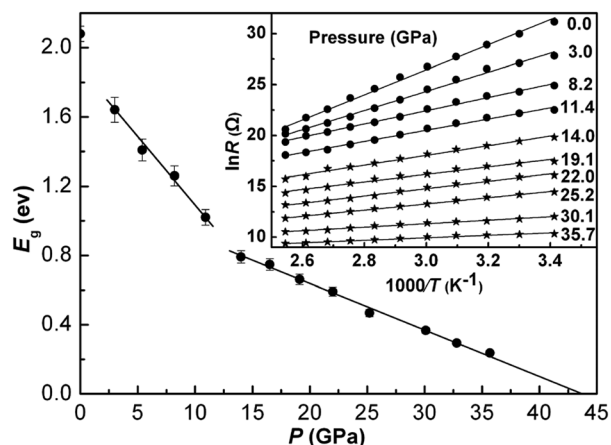


Fig. 6 Pressure dependence of the carrier transport activation energy of AlAs in the bulk transport process. The inset shows the $\ln R$ vs. $1000/T$ curves at different pressures.

14.7 GPa. During decompression, ε_r of AlAs shows similar behavior to the compression process.

Previous band structure calculations predicted that AlAs becomes metallic in the B8 structure.²¹ The temperature dependence of the impedance spectra was investigated to verify whether AlAs becomes metallic in the high-pressure phase. The obtained bulk resistances are plotted in the inset of Fig. 6 in the Arrhenius format. R_b of AlAs decreases with increasing temperature within the pressure range of 0–35.7 GPa, which indicates that AlAs remains semiconductive below 35.7 GPa and is inconsistent with the band structure calculation results.²¹ The inconsistency between our observation and the previously reported band-structure results may be attributed to the underestimation of the band-gap by first-principles calculations.^{34,35} This underestimation has been previously observed with the ambient-pressure band-gap of AlAs.²¹

To gain a deeper insight into the electrical transport behavior of AlAs under compression, we obtained the carrier transport activation energy of the bulk transport process (E_g) by fitting the R - T curves. It was found that the $\ln R$ vs. $1/T$ curves of AlAs match well with the Arrhenius electrical transport model. Hence, we obtained E_g from the Arrhenius equation:³⁶

$$E_g = 2k_B \partial \ln R / \partial (1/T) \quad (2)$$

where R is the high-temperature resistance, k_B is Boltzmann constant, and T is the temperature. E_g represents the carrier electrical transport activation energy in the bulk conduction process. E_g obtained by fitting the ambient pressure R - T curve is 2.08 eV, which is consistent with previously reported band-gap result.³⁷ We therefore consider E_g to be the intrinsic band gap of AlAs. As shown in Fig. 6, E_g decreases with pressure, which indicates that the charge carriers can overcome the band-gap more easily with thermal vibrations, and thereby increase the carrier concentration and further improve the conductivity of AlAs. Above 14.0 GPa, the pressure dependence of E_g varies and then drops gently. Based on the change tendency of E_g with P , we infer that E_g should be close to zero at ~ 45.0 GPa, implying that a further increase in carrier concentration would be small and AlAs would become metallic.

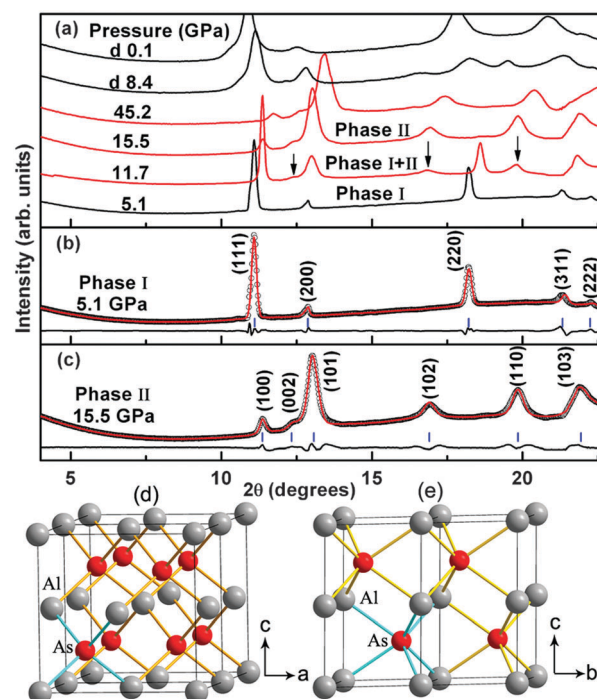


Fig. 7 (a) Representative XRD patterns of AlAs at various pressures. (b and c) Show the Rietveld refinement results for Phase I ($F\bar{4}3m$ structure with $a = 5.552$ Å, Al (0, 0, 0) and As (0.25, 0.25, 0.25), $R_p = 2.03\%$, $\chi^2 = 1.215$) at 5.1 GPa and Phase II ($P6_3/mmc$ structure with $a = 3.615$ Å, $c = 5.769$ Å, Al (0, 0, 0) and As (0.333, 0.667, 0.25), $R_p = 4.12\%$, $\chi^2 = 1.523$) at 15.5 GPa, respectively. (d and e) Are the polyhedral views of AlAs in B3-phase and B8-phase, respectively.

We were motivated to determine the origin behind the boundary- to bulk-dominated electrical transport mechanism conversion and dramatic drops in resistance. Discontinuous changes in electrical transport properties usually coincide with crystal structural transition. High-pressure XRD measurements were conducted to monitor the structural modification of AlAs under compression. Fig. 7a plots the representative XRD patterns of AlAs up to 40.2 GPa. With a gradual increase in pressure up to 11.7 GPa, some new diffraction peaks at $\sim 12.3^\circ$, $\sim 16.9^\circ$ and $\sim 19.8^\circ$ suddenly emerge, which clearly signal the I–II structural transition. Above 15.5 GPa, a single-phase pattern of Phase II appears, indicating the I–II structural transition is complete. Phase II remains stable up to the maximum pressure of 45.2 GPa. Upon quenching to ambient pressure, all the diffraction peaks of Phase I reappear and those of Phase II disappear, indicating that this structural transition is reversible.

With the Rietveld refinement analysis through the GSAS program package (Fig. 7b), the patterns of Phase I can be indexed into a face-centered cubic structure. Moreover, the structure with $F\bar{4}3m$ symmetry matches the patterns better than those with other symmetries, thus showing better agreement with the previously reported results.¹⁶ It was found that structures with $P6_3/mmc$ symmetry (B8, NiAs structure) are more suitable for Phase II (Fig. 7c), which is consistent with the literature observation in ref. 18, whereas different from other studies in which AlAs transforms into the B1 phase at high pressure.^{19–21} This inconsistency is caused by an overestimation of the ground state energy in

the first principles calculations,^{34,35} which increases the difficulty in distinguishing the relative stability of structures, especially the close structures that have subtle energy differences. After examining the structural differences between Phase I and II carefully, we found that this type of structural transition can be attributed to crystal distortion of AlAs. A similar observation was also reported in a previous study.³⁸ The cubic–hexagonal transition gives rise to the generation of two new Al–As bonds, accompanied by the coordination number changing from four-coordinated in the cubic structure to six-coordinated in the hexagonal structure (Fig. 7e). This significantly changes the electronic structure of AlAs, including the band-gap.²¹ Further evidence to support the variation of the energy band-gap can also be found in the change in carrier transport activation energy at ~14.0 GPa (Fig. 6).

The pressure-induced structural transition contributes to understanding the conversion of the electrical transport mechanism from grain boundary- to bulk-dominated and the dramatic reduction of the resistance of AlAs at ~10.9 GPa. For bulk conduction, the cubic–hexagonal structural transition at 11.0–15.0 GPa essentially modifies the electronic structure of AlAs, which decreases E_g and subsequently increases the carrier concentration, and further gives rise to the significant reduction of R_b . During decompression, AlAs recovers to its cubic structure, resulting in the recovery of E_g and carrier concentration. Consequently, R_b returns to the initial value after the pressure is fully released.

In the case of the boundaries' conduction, previous studies have shown that the grain boundaries are composed of disordered atoms and contain large numbers of defects due to incomplete bonding, which usually trap the charge carriers and act as recombination centers, subsequently leaving few free carriers for electrical transport.³⁹ The trapped carriers usually result in boundary scattering effects, which consequently hinder the conduction in the grain boundaries. Under compression, the recombination centers should eventually become saturated with the increase in the number of free carriers due to the decrease in the energy band-gap, and hence no longer trap the free carriers. Consequently, the grain boundary effect becomes much weaker compared with that of bulk conduction. During decompression, AlAs goes back to its original cubic structure below 10.0 GPa, so that the pressure-induced change in electronic structure, reduction of E_g and increase in carrier concentration are recovered. Therefore, the grain boundary effect re-emerges and the electrical transport behavior of AlAs returns to its initial states after quenching to ambient pressure.

The main contributions to the relative permittivity are the atomic and electronic polarization with additional contributions from the microstructure of the sample, including grain size and boundary states of the samples.^{40,41} Thus, the unusual changes in the relative permittivity of AlAs can also cause the pressure-induced structural transition.

4. Conclusions

In summary, by combining the X-ray diffraction and AC impedance spectral measurements, we studied the structural and electrical transport properties of AlAs under compression. The resistances

of both the grain boundaries and bulk vary abnormally at ~10.9 GPa, accompanied by the cubic–hexagonal structural transition of AlAs. With further compression, the boundary effect becomes undistinguished, and subsequently the electrical transport mechanism converts from boundary- to bulk-dominated, which gives rise to significant reduction of the total resistance of AlAs. After quenching to ambient pressure, resistances recover to the initial values followed by the re-emergence of the boundary effect. E_g decreases with increasing pressure and changes its pressure dependence at ~14.0 GPa, which rationalizes the anomalous variation of the electrical transport properties of AlAs. The experimental results indicate that the grain boundary effect can be modulated by compression and plays positive roles in devices such as increasing the difference in resistance between the two states, which opens up new possible pathways for designing AlAs-based applications and may also be applicable in optimizing the performance of phase-change memories.

Acknowledgements

This study was supported by the National Basic Research Program of China (Grant No. 2011CB808204), the National Natural Science Foundation of China (Grant No. 11374121 and 11404133), and the Program of Science and Technology Development Plan of Jilin Province (Grant No. 20140520105JH).

References

- 1 J. H. Schön, S. Berg, C. Kloc and B. Batlogg, *Science*, 2000, **287**, 1022–1023.
- 2 Z. T. Zhu, J. T. Mason, R. Dieckmann and G. G. Malliaras, *Appl. Phys. Lett.*, 2002, **81**, 4643–4645.
- 3 P. Yasaei, B. Kumar, R. Hantehzadeh, M. Kayyalha, A. Baskin, N. Repnin, C. H. Wang, R. F. Klie, Y. P. Chen, P. Král and A. S. Khojin, *Nat. Commun.*, 2014, **5**, 4911.
- 4 Z. Bao, A. J. Lovinger and J. Brown, *J. Am. Chem. Soc.*, 1998, **120**, 207–208.
- 5 J. H. Schön, C. Kloc and B. Batlogg, *Org. Electron.*, 2000, **1**, 57–64.
- 6 L. H. Jimison, M. F. Toney, I. McCulloch, M. Heeney and A. Salleo, *Adv. Mater.*, 2009, **21**, 1568–1572.
- 7 A. W. Tsen, L. Brown, M. P. Levendorf, F. Ghahari, P. Y. Huang, R. W. Havener, C. S. Ruiz-Vargas, D. A. Muller, P. Kim and J. Park, *Science*, 2012, **336**, 1143–1146.
- 8 R. Gerthardt and A. S. Nowick, *J. Am. Ceram. Soc.*, 1986, **69**, 641–646.
- 9 C. Li, Y. Wu, J. Poplawsky, T. J. Pennycook, N. Paudel, W. J. Yin, S. J. Haigh, M. P. Oxley, A. R. Lupini, M. Al-Jassim, S. J. Pennycook and Y. Yan, *Phys. Rev. Lett.*, 2014, **112**, 156103.
- 10 S. I. Kim, K. H. Lee, H. A. Mun, H. S. Kim, S. W. Hwang, J. W. Roh, D. J. Yang, W. H. Shin, X. S. Li, Y. H. Lee, G. J. Snyder and S. W. Kim, *Science*, 2015, **348**, 109–114.
- 11 H. Rupperecht, J. M. Woodall and G. D. Pettit, *Appl. Phys. Lett.*, 1967, **11**, 81–83.
- 12 H. Nelson and H. Kressel, *Appl. Phys. Lett.*, 1969, **15**, 7–9.
- 13 H. Kressel and F. Z. Hawrylo, *Appl. Phys. Lett.*, 1970, **17**, 169–171.

- 14 I. Hayashi, M. B. Panish and P. W. Foy, *IEEE J. Quantum Electron.*, 1969, **5**, 211–212.
- 15 K. N. Tu, J. W. Mayer and L. C. Feldman, *Electronic Thin Film Science for Electrical Engineers and Materials Scientists*, Macmillan, New York, 1992.
- 16 K. H. Hellwege and B. Landolt, *Semiconductors: Physics of Group IV Elements and III–V Compounds*, Springer-Verlag, Berlin, 1982.
- 17 R. G. Greene, H. Luo, T. Li and A. L. Ruoff, *Phys. Rev. Lett.*, 1994, **72**, 2045–2048.
- 18 A. Onodera, M. Mimasaka, I. Sakamoto, J. Okumura, K. Sakamoto, S. Uehara, K. Takemura, O. Shimomura, T. Ohtani and Y. Fujii, *J. Phys. Chem. Solids*, 1999, **60**, 167–179.
- 19 H. Wang, X. Li, C. Li and K. Wang, *Mater. Chem. Phys.*, 2009, **117**, 373–376.
- 20 D. Varshney, G. Joshi, N. Kaurav and R. K. Singh, *J. Phys. Chem. Solids*, 2009, **70**, 451–458.
- 21 A. Srivastav, N. Tyagi, U. S. Sharma and R. K. Singh, *Mater. Chem. Phys.*, 2011, **125**, 66–71.
- 22 R. Schmidt, J. Wu, C. Leighton and I. Terry, *Phys. Rev. B: Condens. Matter Mater. Phys.*, 2009, **79**, 125105.
- 23 Y. Wang, Y. H. Han, C. X. Gao, Y. Z. Ma, C. L. Liu, G. Peng, B. J. Wu, B. Liu, T. J. Hu, X. Y. Cui, W. B. Ren, Y. Li, N. N. Su, H. W. Liu and G. T. Zou, *Rev. Sci. Instrum.*, 2010, **81**, 013904.
- 24 H. K. Mao, P. M. Bell, J. W. Shaner and D. J. Steinberg, *J. Appl. Phys.*, 1978, **49**, 3276–3283.
- 25 A. C. Larson and R. B. Von Dreele, *General Structure Analysis System (GSAS) LAUR*, Los Alamos National Laboratory, New Mexico, 2004.
- 26 M. A. L. Nobre and S. Lanfredi, *J. Appl. Phys.*, 2003, **93**, 5576–5582.
- 27 T. B. Adams, D. C. Sinclair and A. R. West, *Phys. Rev. B: Condens. Matter Mater. Phys.*, 2006, **73**, 094124.
- 28 Y. Q. Li, Y. Gao, Y. H. Han, Q. L. Wang, Y. Li, N. N. Su, J. K. Zhang, C. L. Liu, Y. Z. Ma and C. X. Gao, *J. Phys. Chem. C*, 2012, **116**, 25198–25205.
- 29 A. P. Nayak, S. Bhattacharyya, J. Zhu, J. Liu, X. Wu, T. Pandey, C. Q. Jin, A. K. Singh, D. Akinwande and J. F. Lin, *Nat. Commun.*, 2014, **5**, 3731.
- 30 B. Liu, Y. H. Han, C. X. Gao, Y. M. Zhang, G. Peng, B. J. Wu, C. L. Liu, Y. Wang, T. J. Hu, X. Y. Cui, W. R. Ren, Y. Li, N. N. Su, H. W. Liu and G. T. Zou, *J. Phys. Chem. C*, 2010, **114**, 14251–14254.
- 31 C. X. Gao, Y. H. Han, Y. Z. Ma, A. White, H. W. Liu, J. F. Lou, M. Li, C. Y. He, A. M. Hao, X. W. Huang, Y. W. Pan and G. T. Zou, *Rev. Sci. Instrum.*, 2005, **76**, 083912.
- 32 R. E. Fern and A. Onton, *J. Appl. Phys.*, 1971, **42**, 3499–3500.
- 33 J. J. Liu, C. G. Duan, W. G. Yin, W. N. Mei, R. W. Smith and J. R. Hardy, *Phys. Rev. B: Condens. Matter Mater. Phys.*, 2004, **70**, 144106.
- 34 M. Dadsetani and A. Pourghazi, *Phys. Rev. B: Condens. Matter Mater. Phys.*, 2006, **73**, 195102.
- 35 C. J. Wu, L. H. Yang and L. E. Fried, *Phys. Rev. B: Condens. Matter Mater. Phys.*, 2003, **67**, 235101.
- 36 A. L. Chen and P. Y. Yu, *Phys. Rev. Lett.*, 1993, **71**, 4011–4014.
- 37 B. Monemar, *Phys. Rev. B: Solid State*, 1973, **8**, 5711–5718.
- 38 J. Cai and N. X. Chen, *Phys. Rev. B: Condens. Matter Mater. Phys.*, 2007, **75**, 174116.
- 39 M. M. Mandurah and K. C. Saraswat, *IEEE Trans. Electron Devices*, 1981, **28**, 1163–1170.
- 40 S. García-Martín, A. Morata-Orrantia and M. Á. Alario-Franco, *J. Appl. Phys.*, 2006, **100**, 054101.
- 41 A. Verma and D. C. Dubew, *J. Am. Chem. Soc.*, 2005, **88**, 519–523.